Effect of Temperature on Raman Intensity of nm-thick WS_2: Combined Effects of Resonance Raman, Optical Properties, and Interface Optical Interference

Hamidreza Zobeiri, [a, †] Shen Xu, [b, †] Yanan Yue, [c] Qianying Zhang, [d] Yangsu Xie, [e, *] Xinwei Wang [a, *]

[a] Department of Mechanical Engineering, Iowa State University, Ames, Iowa 50011, United States.

[b] Automotive Engineering College, Shanghai University of Engineering Science, 333 Longteng Road, Shanghai 201620, People's Republic of China.

[c] School of Power and Mechanical Engineering, Wuhan University, Wuhan 430072, People's Republic of China.

[d] College of Metallurgy and Material Engineering, Chongqing University of Science & Technology, [e] University Town, Huxi Shapingba District, Chongqing, 401331, People's Republic of China.

[e] College of Chemistry and Environmental Engineering, Shenzhen University, Shenzhen, Guangdong 518055, People's Republic of China.

[†] H. Zobeiri and S. Xu contributed equally to this work.

Abstract

Temperature dependent Raman intensity of 2D materials features very rich information about the material's electronic structure, optical properties, and nm-level interface spacing. To date, there still lacks rigorous consideration of the combined effects. This renders the Raman intensity information less valuable in material studies. In this work, the Raman intensity of four supported multilayered WS_2 samples are studied from 77 K to 757 K under 532 nm laser excitation. Resonance Raman scattering is observed, and we are able to evaluate the excitonic transition

energy of B exciton and its broadening parameters. However, the resonance Raman effects cannot explain the Raman intensity variation in the high temperature range (room temperature to 757 K). The thermal expansion mismatch between WS_2 and Si substrate at high temperatures (room temperature to 757 K) makes the optical interference effects very strong and enhances the Raman intensity significantly. This interference effect is studied in detail by rigorously calculating and considering the thermal expansion of samples, the interface spacing change, and the optical indices change with temperature. Considering all of the above factors, it is concluded that the temperature dependent Raman intensity of the WS_2 samples cannot be solely interpreted by its resonance behavior. The interface optical interference impacts the Raman intensity more significantly than the change of refractive indices with temperature.

Keywords: 2D materials, temperature dependent Raman, excitonic transition energy, thermal expansion, interface optical interference

1. Introduction

Thin two-dimensional transition metal dichalcogenides (2D TMDs) in the form of MX_2 (M = Mo, W and X = S, Se) have been the topic of large number of studies due to their various extraordinary electrical, mechanical, and optical properties [1]. In comparison with graphene, MX_2 TMDs are semiconductors with intrinsic band gap that undergoes a transition from indirect in bulk to direct in single layer material due to the quantum confinement effects [2-6]. This tunable band gap energy, as well as large exciton binding energy [7], clear spin-splitting of the valence band [8], and high photoluminescence efficiency [9], make TMDs an attractive candidate for various optoelectronic applications and field effect transistors [10-12]. Besides the aforementioned properties, TMDs are among the most stable 2D materials [13]. The weak van der Waals (vdW) force between atomic layers is another interesting feature of these materials. These weakly bonded layers can be easily mechanically exfoliated and stacked with other TMDs to prepare several kinds of heterostructures [14, 15].

Raman spectroscopy has proved to be one of the most promising non-destructive tools to characterize thermal, structural, and electrical properties of 2D materials [16-20]. The temperature and laser power dependence of Raman shift of main TMDs' Raman peaks are explored in several previous works to characterize thermal conductivity [21-24], hot carrier diffusion coefficient [25, 26], and thermal expansion coefficient [27-29]. Late *et al.* observed a linear relationship between temperature and Raman peak position of single- and few-layered $MoSe_2$ and WSe_2, which is related to thermal expansion and anharmonicity [27]. Sahoo *et al.* determined the thermal conductivity of suspended few-layered MoS_2 using the temperature dependent Raman studies of A_{1g} and E_{2g} modes [22]. Bhatt *et al.* conducted a low temperature dependent Raman investigation on TMDs and determined

Grüneisen parameters [30]. Although the temperature dependence of Raman shift of TMDs has been considerably studied, few works have been reported on temperature dependence of Raman intensity of TMDs' Raman peaks. Temperature dependence study of Raman intensity makes the investigation of resonance Raman scattering possible. In fact, there are two ways to performing resonance Raman study, either by changing the sample's temperature or changing the photon energy of irradiating laser. Resonance Raman takes place when the radiation photon energy equals electronic absorption band and causes the Raman intensity to be enhanced by several orders of magnitude. Resonance Raman spectroscopy makes it possible to study the electronic information for a molecule by providing more intense Raman spectra near selected Raman bands. This potential is more helpful when investigating materials with weak nature of normal Raman spectra, such as proteins, nucleic acids, and water [31]. In resonance Raman, the closer the photon energy of the irradiating laser is to the energy related to electronic transition, the higher will be the Raman intensity. It should be noted that the difference between the laser photon energy and electronic transition energy will never be zero due to the finite width of the absorption band. As a result, the Raman intensity cannot rise to infinity. The light scattering theory gives the intensity of Raman scattering as [31]:

$$I = Kl\alpha^2\omega^4, \tag{1}$$

where K is a constant that consists of several other constants, like speed of light. l and ω are intensity of incident light and frequency of the irradiating laser, respectively. α indicates the polarizability of electrons in a molecule. There are several ways to describing the polarizability, such as time-dependent perturbation theory [32]. Based on this theory and Eq. (1), we have [32, 33]:

$$\alpha \propto \left| \frac{\langle F|H_{e-ph}(\omega_s)|I'\rangle\langle I'|H_{e-p}|I\rangle\langle I|H_{e-ph}(\omega_i)|G\rangle}{(E_{iI} - E_i - i\Gamma_1)(E_{I'F} - E_s - i\Gamma_2)} \right|^2, \tag{2}$$

where $|F\rangle$, $|G\rangle$, and $|I\rangle$ (or $|I'\rangle$) are final, initial (ground), and intermediate states, respectively. ω_i (or ω_s) indicates the frequency of the incident (or scattered) photon. $H_{e\text{-}ph}$ and $H_{e\text{-}p}$ are electron-photon and electron-phonon interactions Hamiltonians, respectively. Also, the energy difference between initial and intermediate (or intermediate and final) states is indicated by E_{iI} (or $E_{I'F}$). Γ_1 and Γ_2 are the line width of excited states during scattering (damping constants) that are related to the lifetime of the excited states at each temperature. Finally, E_i (or E_s) is the energy of incident (or scattered) light which is defined as $h\omega_i$ (or $h\omega_s$). Based on the position of intermediate states, E_{iI} (or $E_{I'F}$) could represent band gap or excitonic excitation gap at each temperature. Resonance Raman takes place when these band energies are very close to E_i (or E_s). In case the main intermediate state is the 1s exciton state that contributes to Raman scattering in TMDs, and considering Eq. (1) and Eq. (2), the Raman intensity could be written as [33]:

$$I \propto \left| \frac{1}{[E(T) - E_i - i\Gamma(T)][E(T) - E_s - i\Gamma(T)]} \right|^2 . \quad (3)$$

Here $E(T)$ and $\Gamma(T)$ are exciton's temperature dependent transition energies and damping constants, respectively. Note that in a specific resonance Raman experiment, K, l, and ω in Eq. (1) are held constant. Also, the numerator of Eq. (2) is considered constant. Considering the equations above, resonance Raman spectroscopy is a powerful tool to study the electronic properties of TMDs.

Gaur *et al.* studied the resonance Raman scattering of 1L and bulk WS_2 by changing the temperature from 83 to 583 K. They observed more intense second-order Raman bands with B exciton on monolayer WS_2 than bulk under resonance condition. In addition, the intensity of 2LA(M) Raman peak is observed to be maximum at room temperature (RT) due to the wider difference between incident laser energy and band gap energy at higher or lower temperatures than

RT [34]. Huang *et al.* reported the same observation using supported monolayer WS_2 sample on silicon substrate [29]. They observed that the energy of B exciton is resonant with the energy of 514.5 nm wavelength laser, and the maximum laser intensity emerges at a temperature close to 223 K. In another work, Fan *et al.* performed a resonance Raman scattering study of bulk and monolayer MoS_2 and bulk TMDs using different laser energies and the resonance was tuned by varying the sample temperature [33]. For WS_2 and MoS_2, the resonance energies coincide with A and B exciton's energy, while for WSe_2 resonance Raman was observed in a wider range of energy and could not be explained with its excitonic energies [33].

Besides the sample temperature that affects the electronic band structure and subsequently intensity of the Raman mode, the optical properties of a material and their evolution with the temperature could also influence the Raman intensity. Cherroret *et al.* investigated the effects of temperature on refractive index of semiconductors and its relationship with the band structure, as well as the thermal expansion [35]. For supported samples on a substrate, naturally there is a spacing air gap layer between the sample and substrate that contributes to the Raman intensity due to the multi-reflections that happen in this layer, and increases the intensity of the scattered light [36].

In this work, we study the temperature-dependent Raman intensity of nm-thick WS_2 samples. By varying the temperature from very low (77 K) to very high values (757 K), we are able to observe the resonance Raman of the E_{2g} and A_{1g} Raman modes. The Raman intensity of the A_{1g} mode at several temperatures is used to study the excitonic transition energy and broadening parameter of the four WS_2 samples under the resonance Raman condition. Then, since the resonance Raman is not the sole phenomenon that affects the Raman intensity (I), other phenomena that contribute to

the value of *I* are studied. Optical interference and change in optical properties against temperature are the other main factors that influence *I*. To analyze these effects, a multi-reflection model is constructed and analyzed to include the aforementioned effects. Also, thermal expansion of the WS_2 samples over a wide temperature range is estimated. It is discovered that for the supported samples under resonance condition, the Raman intensity carries the information about all of the above factors significantly, and each of them needs to be considered in the Raman study.

2. Experimental Details and Structure of Samples

Temperature dependent Raman measurement is conducted using a BWTEK Voyage confocal Raman system. A 532 nm continuous wave laser (Excelesior-532-150-CDRH, Spectra-Physics) is used to excite the Raman signal. In this work, a 20× objective lens is used to focus the laser spot on the WS_2 sample. Using this CW laser and a 20× objective lens, the laser spot radius is around 1.4 μm. An optical cell chamber is used to control the temperature of the sample. Rapid inlet and outlet of N_2 gas allows us to control the temperature inside the chamber. More information about this Raman system and cell chamber could be found in our previous works [37, 38].

Three few-layered and a bulk WS_2 samples are prepared using the mechanical exfoliation method and transferred to the silicon substrate. This method has been used extensively in our past works for 2D sample preparation, and details of the preparation process can be found in those works [39, 40]. Figure 1 shows the AFM images of these four supported samples. Figure 1(a1-d1) show the 2D images of these samples. The boundary area of the WS_2 sample and Si substrate is used to measure the sample thickness. 3D AFM images over a 20 μm × 20 μm area are shown in Figure 1(a2-d2) to display the wrinkles on and the bubbles underneath the samples. As shown in these four 3D

images, the first sample with 13 nm thickness is the least flat one and more cracks can be observed on its surface. The thickness profile of each sample is indicated in Figure 1(a3-d3). Thickness measurement is conducted along the direction of the dashed arrow in Figure 1(a1-d1). To check the sample's flatness, the roughness of WS_2 layer is measured over the area that the laser spot is located. These locations are displayed using dotted arrows in 2D AFM images and roughness profiles are shown in Figure 1(a4-d4). Δl_{max} represents the biggest thickness variation along the dotted arrow. For all of the samples, Δl_{max} is less than 15% of the sample thickness which shows the flatness of each layer. The bulk WS_2 shown in Fig. 1 has a thickness of 673 nm, which is thick enough that the Raman laser light will not penetrate to induce optical interference effect.

3. Absolute Raman Intensity Variation with Temperature: Resonance Raman Scattering

A room temperature Raman spectrum of a bulk WS_2 film supported on Si substrate over the range of 100-750 cm^{-1} is shown in Figure 2. Bulk WS_2 belongs to D_{6h}^4 point group and has 18 vibrational modes at the center of hexagonal Brillouin zone (Γ), as [41, 42]:

$$\Gamma = A_{1g} + (2B_{2g}) + E_{1g} + 2E_{2g} + 2A_{2u} + (B_{1u}) + 2E_{1u} + (E_{2u}). \quad (4)$$

Several first-order and second-order modes are observed. First-order peaks include LA(M), LA(K), $E_{2g}^1(\Gamma)$, $E_{2g}^2(\Gamma)$, and $A_{1g}(\Gamma)$. Other observed peaks are second order modes that can be combinations of other first-order modes, like $4LA(M)$. Another peak (P_9) at 525 cm^{-1} is assigned to the Si substrate. Rest of the peaks can be interpreted as the combination of optical and acoustic modes. The 2LA(M) mode is a second-order longitudinal acoustic mode and its frequency is 348 cm^{-1} under 532 nm laser irradiation. This frequency is very close to the frequency of the $E_{2g}^1(\Gamma)$ mode, and it causes the overlapping of the two peaks, as shown in Figure 2. Therefore, it is not possible to use the multi-peak Lorentzian fitting method to distinguish these two peaks exactly

using our Raman spectrometer with a spectral resolution of 1.9 cm^{-1} at Raman shifts in proximity of these two peaks. Here, we use the $A_{1g}(\Gamma)$ Raman active mode, and the very strong peak at 352 cm^{-1} which is a combination of both 2LA(M) and $E^1_{2g}(\Gamma)$ peaks to perform our analysis. The $A_{1g}(\Gamma)$ Raman peak represents the out-of-plane vibrations of sulfur atoms, while 2LA(M) and $E^1_{2g}(\Gamma)$ modes are associated with the in-plane vibrations of tungsten and sulfur atoms. These vibration modes are represented in Figure 2. It should be noted that the resulting Raman peak of both 2LA(M) and $E^1_{2g}(\Gamma)$ modes is stronger than each of them due to the similar vibrational direction of these two modes, while depending on the temperature, each peak's contribution to the resulting peak could be different. This effect will be further discussed in the following sections.

As mentioned earlier, resonance Raman effect occurs when the energy of irradiating laser beam is close to the electronic transition of an exciton. In case of bulk and nm-thick WS_2 samples, electronic transition energies of A and B excitons at room temperature are close to 1.9 and 2.4 eV, respectively [43, 44]. The energy gap for B exciton is very close to the photon energy of the 532 nm laser (2.33 eV). The excitonic gaps can be tuned and modified by manipulating external parameters, such as temperature and pressure [45]. Therefore, it is possible to change the sample's temperature to tune the energy of B exciton in order to resonate with the exciting laser at 2.33 eV. Raman spectra of such a study for the bulk WS_2 is shown in Figure 3. As shown in Figure 3(a), the Raman intensity of the two peaks increases as the temperature increases from 77 K to around 360 K where resonance Raman occurs, and starts to decrease after that. This effect is also shown as 2D contour of Raman intensity against temperature [Figure 3(b)]. In fact, as the temperature increases, the energy of the B exciton approaches the energy of the incident laser and resonance Raman happens.

And as the temperature further increases, the transition energy of B exciton deviates from the photon energy of the laser light and Raman intensity decreases. This observation is in very good agreement with Eq. (3) and will be analyzed in detail later.

Figure 4 shows the normalized Raman intensity (I^*) and Raman shift of the two modes versus temperature for all samples studied in this work. I^* is the absolute Raman intensity divided by laser power and integration time for the Raman experiment of each sample. The resonance Raman behavior is obvious in Figure 4(a) and (b) for both $E^1_{2g} + 2LA(M)$ and A_{1g} peaks, respectively. Laser power and integration time values of each sample are summarized in Table 1. Note this laser power is just before irradiating the sample and includes all the transmission effects of the Raman system, such as objective lens and glass window of optical cell chamber. It should be noted that under 20× objective lens, these laser powers are the minimum values required to collect a good-quality Raman peaks of both modes that could be fitted with high accuracy, and further decrement of the laser power will damage the data fitting. This effect is more significant at low temperatures. Also, in this work, 20× objective lens is used to cover a larger area of the sample compared to 50× or 100× objective lens. Under higher magnification lenses with smaller laser spot size, the Raman intensity can be different at various locations of the sample because the laser spot size is comparable to the lateral size of the sample roughness. By using 20× objective, we can make sure that the Raman intensity of different surface characters are included in our Raman measurement. The Raman intensity of $E^1_{2g} + 2LA(M)$ mode has a non-zero value at very low temperatures and reaches the maximum at room temperature, and it goes to very low values at very high temperatures [Figure 4(a)]. In contrast, the Raman intensity of A_{1g} mode possess a very low value (close to zero) at low temperatures and increases with the increased temperature, until it reaches

the maximum value at around 420 K. I^* then decreases against increased temperature at higher temperatures, but this decrease of I^* is less compared with that of $E^1_{2g} + 2LA(M)$ mode's behavior at high temperatures [Figure 4(b)]. Therefore, there are two main differences between the I^* changes versus temperature for the two modes, which are the shape of the curve at very high or very low temperatures and location of the peak.

First, the 2LA(M) acoustic mode is stronger at lower temperatures and contributes more to the combined mode and its effects become less significant as temperature takes higher values [29]. This could also be understood by studying the Raman peak position versus temperature relation, as shown in Figure 4(c). As shown in this figure, Raman peak position of this curve starts to increase at higher temperatures, which shows more significant contribution of E^1_{2g} peak at these temperatures. As shown in Figure 4(d), the temperature dependence of A_{1g} mode peak position is decreasing linearly with a temperature coefficient ~-0.012 $cm^{-1} \cdot K^{-1}$ for all samples that is very close to reference values [29, 46]. At the temperatures higher than the peak location in Figure 4(a) and (b), the Raman intensity of A_{1g} mode decreases with a much slower pace in comparing to the $E^1_{2g} + 2LA(M)$ mode. This difference could be attributed to the different effects of thermal expansion on Raman intensity of each mode. In fact, the thermal stresses at higher temperatures can lead to forming of wrinkles in WS_2 sample due to the different thermal expansion coefficients of WS_2 and Si substrate. As reported in previous works, A_{1g} mode is more sensitive to these effects than the $E^1_{2g} + 2LA(M)$ mode and is affected stronger. Another factor that can be resulted from this thermal expansion mismatch between WS_2 sample and substrate is the optical effects and how it causes the increase in Raman intensity. Another point that needs to be noted is the difference

between the Raman intensity of each mode for different samples. It is shown that I^* increases as the thickness of sample increases. These two last effects will be discussed in next sections.

As shown in Eqs. (2) and (3), resonance Raman effect depends on both $E(T) - E_i$ and $E(T) - E_s$, which are related to incident light and scattering light. This effect is well considered in our fitting calculation, as shown in next section. Raman shifts of the $E^1_{2g} + 2LA(M)$ and A_{1g} modes are around 350 cm^{-1} and 420 cm^{-1}, respectively. Therefore, the calculated E_s based on each of these two modes is about 2.287 eV and 2.279 eV, respectively. These two values are very close and using them we can estimate the temperature difference between the location of I^*-T curve of each mode based on these E_s values using the calculated values of excitonic transition energies which are calculated in the following section. This temperature difference between the location of two peaks is less than 30 K. While the actual difference between the peak locations, as shown in Figure 4(a) and (b), is more than 50 K. So, there should be other reasons that are contributing to this phenomenon. Here we discuss about the potential reasons. Again, one reason could be the effect of 2LA(M) mode in fitting the Raman intensity of the combined $E^1_{2g} + 2LA(M)$ mode. Especially at temperatures lower than 400 K, this acoustic mode is intense and affects the intensity of the combined $E^1_{2g} + 2LA(M)$ peak more. The other reason could be the effect of thermal expansion on Raman intensity of each mode. As we know, the existence of thermal expansion will lead to decrement of Raman intensity by increasing the phonons' energy. This effect is more significant in the A_{1g} mode since its thermal expansion coefficient is larger than the E^1_{2g} mode [29]. On the other hand, we expect that thermal expansion of the sample will increase the thickness of the air gap layer between the WS_2 film and substrate, and leads to increment of the Raman intensity due to

the interface optical interference effect that will be discussed in the next sections.

Table 1. Laser power and integration time used in performing the temperature dependent Raman experiment.

Sample thickness (nm)	Laser power (mW)	Integration time (s)
13	4.56	3
38	1.77	1
45	4.56	3
Bulk	3.99	1

As mentioned in the introduction part and shown by Eq. (3), Raman intensity at each temperature depends on excitonic transition energy (E) and damping constant (Γ) at that temperature. The temperature dependence of E_B (electronic transition energy of B exciton) for low and midrange temperatures (< 360 K) can be expressed using the Varshni empirical relationship as [47, 48]:

$$E_B(T) = E_B(0) - \frac{\alpha_B T^2}{(\beta_B + T)}, \tag{5}$$

where $E_B(0)$ is the electronic transition energy of B exciton at 0 K. α_B and β_B are Varshni coefficients and are related to the electron (exciton)-phonon interaction and Debye temperature. Note that under non-resonance condition, the temperature dependence of excitonic transition energies could be expressed by the Bose-Einstein thermal factor [43]. In this case and under resonance condition, resonance Raman contributes more to the intensity of Raman signal than the phonon thermal population [33]. The temperature dependence of the broadening parameter (Γ) of B exciton is given by [49, 50]:

$$\Gamma_B(T) = \Gamma_{B0} + \frac{\Gamma_{Bph}}{[\exp(\Theta_{Bph}/T) - 1]}. \quad (6)$$

Here Γ_{B0} represents the temperature independent width which is caused by mechanisms like *e-e* interaction, impurity, and dislocation [43]. Γ_{Bph} indicates the electron (exciton)-phonon coupling strength and Θ_{Bph} is the phonon temperature. It is possible to find the electronic properties of WS_2 samples as shown in Eqs. (5) and (6) by fitting the temperature dependent I^* [Figure 4(a) and (b)] in the low temperature range (below ~360 K) [48]. Here, the Raman intensity of A_{1g} mode is used to perform this fitting. Note that since the data of E^1_{2g} mode is combined with the 2LA(M) mode, it is not accurate enough to use them for finding the electronic properties. Figure 5(a) shows the fitting result for all the four samples. Figure 5(b) indicates the temperature evolution of excitonic transition energy and broadening parameter. As shown in this figure, *E* decreases with increased temperature for all samples, while Γ increases as temperature increases. Table 2 includes the fitted parameters as indicated in Eqs. (5) and (6). These values are in very good agreement with the reference values of transition and damping energies, and Debye temperature of WS_2 [33, 43]. Especially, the transition energy at 0 K and Debye temperature are around 2.4 eV and 220 K, respectively, which is close to the reference values of B excitons of WS_2 as 2.5 eV and 200 K, respectively [43]. However, the discrepancies observed in other columns could be resulted from different factors, such as different structure of the samples and subsequently different defect effects, fitting uncertainties which is caused by experimental uncertainty at lower temperatures, and interface optical interferences that can affect the Raman intensity of each mode.

Table 2. Results of the fitting of the Raman intensity of the A_{1g} peak versus temperature curves for all four WS_2 samples.

Sample thickness (nm)	$E_B(0)$ (eV)	α_B (meV·K^{-1})	β_B (K)	Γ_{B0} (meV)	Γ_{Bph} (eV)	Θ_{Bph} (K)
13	2.496	0.996	190.85	35.75	0.795	752.67
38	2.392	0.430	211.85	18.81	0.189	712.71
45	2.412	0.601	229.85	29.00	0.193	684.12
Bulk	2.436	0.672	240.92	25.58	0.499	762.57

So far, the temperature dependent intensity of the Raman signal of four WS_2 samples is discussed as well as the effects of the resonance Raman. While, it should be noted that the Raman intensity at each temperature depends on the optical properties of the sample at that temperature. As shown in Figure 1 which represents the AFM images, it is obvious that the top of the WS_2 layer is not totally flat, and at least ~1 nm roughness exists. It is physically reasonable to claim that the bottom surface of the WS_2 layer has the similar roughness. Therefore, we can expect that there is a default air gap layer between the WS_2 layer and substrate, even without any laser heating. Additionally, the thermal expansion mismatch between WS_2 and Si substrate will cause a wider air gap layer between them, and this effect is more significant at higher temperatures. This spacing caused between the two materials will lead to multi-reflection of incoming laser light and result in the higher laser absorption. This air-gap effect, at this moment, is extremely difficult to separately characterize. However, it has been addressed dramatically and confirmed by comparing the Raman intensity temperature measurement and Raman shift and linewidth based temperature measurement in the study of graphene-Si interface and MoS_2-Si interface. Tang *et al.* showed that the stress-induced Raman shift of graphene on Si substrate is less than 0.1 cm^{-1}, which suggests an

extremely loose mechanical coupling between the two materials [51]. This loose contact makes it possible for the thin layer (graphene) to expand at reduced temperature and causes a wider air gap layer between two materials. Also, Yuan *et al.* studied the interfacial thermal conductance (G_k) between few to tens of layered-MoS_2 and Si substrate and found that G_k at room temperature increases with increased layer number of MoS_2 [39]. Their measured Raman intensity intends to be much higher than that predicted by optics modeling for thinner MoS_2, demonstrating the very strong interface spacing effect for thinner 2D materials. Therefore, it is necessary to consider these two effects when studying the temperature dependent Raman intensity of WS_2 samples.

4. Bulk-normalized Raman Intensity Variation with Temperature: Effect of Optical Properties and Interface

In order to investigate the effect of optical properties of the sample and Si substrate, like refractive index that changes with temperature, the temperature dependent Raman intensity of 13 nm, 38 nm, and 45 nm samples is normalized using the Raman intensity of bulk sample at each temperature and is indicated as I_N^*. Temperature dependent I_N^* is shown in Figure 6 for both $E_{2g}^1 + 2LA(M)$ [Figure 6(a)] and A_{1g} [Figure 6(b)] modes. Note that Raman intensity of bulk is used to normalize the data as it has no interface optical interference effect. For the A_{1g} mode of WS_2, as shown in Figure 6(b), I_N^* increases from low temperatures gradually until it reaches a maximum value at temperatures close to 340 K. Then, it slowly decreases at temperatures go higher and reaches a constant value that is shown using the dotted arrows. This gradual decreasing trend and reaching a constant value is attributed to the effect of optical properties *n* (refractive index) and *k* (extinction coefficient) variation with temperature. Both *n* and *k* increase with increased temperature [35], and as it will be shown, it results in decreased I_N^*. This trend is less obvious for the 13 nm sample,

which is probably due to offset effect by the interface spacing. In fact, the thermal expansion of WS_2 is more than that of the Si substrate and this difference increases by increased temperature. The difference in thermal expansion of two materials at higher temperatures causes wider interface between them. As a result, the Raman intensity increases as the interface spacing becomes larger between WS_2 layer and Si substrate, which is in opposite direction of the effect of *n* and *k* at higher temperatures. Details of the effects of interface spacing and Raman intensity will be discussed in the next section. It should be noted that the normalized intensity (I_N^*) includes all the effects of optical properties (*n* and *k*) and interface spacing, which are very challenging to distinguish through the experiment. In the following section, all these effects are investigated in detail.

Figure 6(a) shows I_N^* of combined $E_{2g}^1 + 2LA(M)$ mode as a function of temperature. Although it includes two modes, its trend is very similar to the A_{1g} mode that shows the interface spacing effects. Optical effects theory applies to this combined mode as well. One main difference between I_N^* of $E_{2g}^1 + 2LA(M)$ mode and A_{1g} mode is: I_N^* of $E_{2g}^1 + 2LA(M)$ mode does not decrease all the way at temperatures higher than 340 K, and this observation could be attributed to the fact that this mode is a combination of both acoustic and optical modes and it is expectable to follow different trend. In summary, comparing both figures, it can be seen that the average I_N^* value of each sample that is shown by dotted arrows is almost equal for both $E_{2g}^1 + 2LA(M)$ and A_{1g} mode. This observation confirms the idea that I_N^* does not include any effect of resonance Raman.

5. Separated Effects of (*n*, *k*) and Interface Spacing on Raman Intensity

5.1. Effect of interface optical interference

As mentioned in the previous section, there are two other main factors besides the resonance

Raman effect that contribute to the Raman intensity variation of each mode against temperature: change in optical properties of WS_2 and Si, and change of spacing between them. It is worth noting that the optical effect will remain significant even if we use suspended samples instead of supported ones. In fact, the suspended sample cannot be completely flat over a hole (or any other configuration that guarantees the suspension), and the center of the sample will be gravitated downward to the hole and will have a cone-like shape. Also, the shape of the suspended sample will be changed at higher temperatures due to thermal expansion, and optical configuration (both absorption and reflection) inside the sample will be altered. This will lead to change in Raman intensity against temperature. Furthermore, when the sample is suspended and cannot freely expand, the stress effects on Raman intensity will be important too, and need to be taken into consideration.

A multi-reflection model is constructed to investigate both effects, as shown in inset of Figure 7(b). The left side of the white dotted line indicates the multi-reflections of the laser light when it passes through the WS_2 layer, air layer and reaches Si substrate. This air layer represents the spacing between the WS_2 layer and substrate which is thicker at higher temperatures. The multiple reflections that take place between several layers result in multiple absorption by the WS_2 sample. The net amount of laser absorption at distance y from the WS_2 top surface can be calculated as [52]:

$$F_{abs.} = T_1 \frac{[1 + r_2 r_3 e^{-2i\beta_2}]e^{-i\beta_y} + [r_2 + r_3 e^{-2i\beta_2}]e^{-i(2\beta_1 - \beta_y)}}{1 + r_2 r_3 e^{-2i\beta_2} + [r_2 + r_3 e^{-2i\beta_2}]r_1 e^{-2i\beta_1}}, \quad (7)$$

where $r_1 = (n_0 - n_1)/(\tilde{i}$, $r_2 = (\tilde{i}$ $\tilde{}$ $\tilde{}$ $\tilde{}$, $r_3 = (\tilde{i}$ $\tilde{}$ $\tilde{}$ $\tilde{}$, and $T_1 = 2n_0/(\tilde{i}$ are the Fresnel reflection and transmittance coefficients, respectively. n_0, $\tilde{i}$, and $\tilde{i}$ are refractive indices of air, WS_2, and Si, respectively. Other coefficients are defined as:

$\beta_y = 2\pi y\tilde{i}$, $\beta_1 = 2\pi t_1\tilde{i}$, and $\beta_y = 2\pi t_2\tilde{i}$, where t_1 and t_2 are the thickness of WS_2 layer and air gap, respectively. Note that λ indicates the wavelength of the incident laser light which is 532 nm in this work.

The right side of the dotted line in inset of Figure 7(b) represents the multi-reflections during the Raman scattering process. This part of the figure shows that even the scattered light inside the WS_2 layer (indicated by black dotted arrows) experiences several reflections that lead to a higher intensity of the Raman signal. The enhancement factor of the scattered light can be calculated similar to Eq. (7) as [52]:

$$F_{sc.} = T_{1,s}\frac{[1+r_{2,s}r_{3,s}e^{-2i\beta_{2,s}}]e^{-i\beta_{y,s}} + [r_{2,s}+r_{3,s}e^{-2i\beta_{2,s}}]e^{-i(2\beta_{1,s}-\beta_{y,s})}}{1+r_{2,s}r_{3,s}e^{-2i\beta_{2,s}} + [r_{2,s}+r_{3,s}e^{-2i\beta_{2,s}}]r_{1,s}e^{-2i\beta_{1,s}}}, \quad (8)$$

where subscript "*s*" is used to show that all of the coefficients used in this equation are calculated based on the wavelength of the scattered light. Finally, the total enhancement factor is calculated as: $F = \int_0^{t_1} |F_{abs.}F_{sc.}|^2 \, dy$. All of the optical and physical properties that are involved in Eqs. (7) and (8), especially $\tilde{i}$, $\tilde{i}$, and t_2, are temperature dependent and affect the ultimate value of *F*. Therefore, it is necessary to include all these effects in our analysis.

5.2. Thermal expansion determination

As mentioned earlier, the thermal expansion mismatch between WS_2 layer and Si substrate causes the spacing between them. So, it is necessary to know the thermal expansion coefficients of the two materials at different temperatures to estimate the local air gap thickness. The inset of Figure 7(a) shows this phenomenon. Here, a one-dimensional (linear) expansion due to the temperature

rise of the WS_2 and Si through an area with 10 μm diameter is considered to estimate their spacing at temperatures higher than 300 K. Since the thermal expansion coefficient of WS_2 is larger than that of Si, an air gap layer emerges and becomes larger at higher temperatures. It is assumed that the shape of this air gap layer follows the laser beam energy distribution and has a Gaussian form [inset of Figure 7(a)]. To simplify the analysis without losing generality of conclusion, the air gap layer in our optical calculation is assumed to be constant along this line, therefore the average value of the Gaussian shape of the spacing is used to estimate the thickness of air layer (t_2). The linear thermal expansion coefficient of bulk silicon from references [53, 54] is used for analysis.

In order to determine the thermal expansion coefficient of the WS_2 samples, a physical model is used that relates the temperature dependent Raman shift of a specific Raman mode to the thermal expansion coefficient and three- and four-phonon anharmonic effects, as below [55]:

$$\omega(T) = \omega_0 + \Delta\omega_{TE} + \Delta\omega_A + \Delta\omega_M, \tag{9}$$

where ω_0 is the Raman shift at 0 K. Also, $\Delta\omega_{TE}$ and $\Delta\omega_A$ are changes in the Raman shift of the specific mode caused by thermal expansion and anharmonic effects, respectively. $\Delta\omega_M$ represents the frequency change due to the thermal expansion mismatch between the WS_2 and Si. For bulk and multilayer samples, $\Delta\omega_M$ is negligible in comparison to the other terms [29]. The Grüneisen constant model describes the term $\Delta\omega_{TE}$ as [56]:

$$\Delta\omega_{TE}(T) = \omega_0[\exp(-N\gamma\int_{T_0}^{T}\alpha_{WS_2}dT) - 1]. \tag{10}$$

Here N, γ, and α_{WS_2} are degeneracy of the Raman mode, Grüneisen parameter, and volumetric thermal expansion coefficient, respectively. This term indicates that vibrational frequency mitigates as the sample expands more due to temperature rise. N takes 2 for the E^1_{2g} mode, and 1

for the A_{1g} mode. In this work, since the E^1_{2g} and 2LA(M) modes are combined, only the temperature dependent Raman shift of the A_{1g} mode is used to calculate the thermal expansion coefficient. T_0 in Eq. (10) is set as the lowest experimental temperature and is equal to 77 K. Here, the relationship between α, γ, and temperature is defined as:

$$\alpha_{WS_2} = \frac{A + BT}{\gamma} = c_0 + c_1 T, \tag{11}$$

where A and B are fitting constants. This linear relationship between α_{WS_2} and T simplifies the fitting process drastically, while it does not damage the accuracy of the calculation. Since we only consider the samples elongation at temperatures higher than 300 K, this linear temperature dependent assumption of α_{WS_2} is reasonable. However, as it is shown in other works [29, 55, 57], α_{WS_2} experiences a non-linear behavior at low temperatures. For temperatures below 300 K, the thermal expansion mismatch will not induce WS_2-Si spacing due to the fact they will contract instead of expand.

The next term, $\Delta\omega_A$, represents the contribution of the creation of an optical phonon and its decay to two, three, or more phonons via anharmonicity. Basically, the incident photons irradiate the sample and cause the creation of the optical phonons. Each optical phonon's decay leads to the creation of two or three phonons (or more). The later one is called four-phonon process, and the former one is three-phonon process [58]. This term, which is related to pure temperature effects, could be expressed as [58]:

$$\Delta\omega_A = C\left(1 + \frac{2}{e^x - 1}\right) + D\left[1 + \frac{3}{e^y - 1} + \frac{3}{(e^y - 1)^2}\right], \tag{12}$$

where C and D are constants that are estimated by fitting the Raman shift change against

temperature. The first term at the right hand side of this equation corresponds to the coupling of an optical phonon to two identical phonons, and the second term indicates the coupling to three identical phonons. Parameters x and y are defined as: $x = \hbar$, $y = \hbar$, where k and $\hbar$ are Boltzmann constant and Planck's constant, respectively.

Eqs. (9-12) are used to fit the temperature dependent frequency shift of the A_{1g} peak [Figure 4(d)]. Figure 7(c-f) show the result of the fitting process, and the extracted fitting parameters are summarized in Table 3.

Table 3. The fitting parameters c_0, c_1, C, D, and ω_0 for A_{1g} mode of four WS_2 samples.

Sample thickness (nm)	c_0 ($\times 10^{-5}$, K^{-1})	c_1 ($\times 10^{-8}$, K^{-2})	C (cm^{-1})	D (cm^{-1})	ω_0 (cm^{-1})
13	1.714	2.422	-2.788	-0.288	428.71
38	0.892	4.590	-3.219	-0.719	428.28
45	2.031	1.636	-2.714	-0.214	428.78
Bulk	1.848	2.210	-2.798	-0.298	428.71

Regarding the fitting parameters C, D, and ω_0 as summarized in Table 3, it is shown that for the 13 nm, 45 nm, bulk sample, they are very close to each other. This is reasonable since for the multilayer and bulk samples it is expected to have similar anharmonic effects. While for the 38 nm sample, these parameters are somehow different from the other samples. It could be caused by several reasons: First, it was assumed that the thermal expansion coefficient of the WS_2 sample changes linearly with temperature, while this assumption may not be accurate enough for the 38 nm sample, especially that we can see the non-linear trend of the frequency shift against temperature for this sample is more significant than the other ones [Figure 7(d)]. Therefore, it is

needed to add more term to equation (11) for this sample, for instance it can be: $\alpha_{WS_2} = c_0 + c_1 T + c_2 T^2$. Second, as mentioned earlier, we made the assumption that the effects of the thermal expansion mismatch between WS_2 layer and Si substrate is negligible. It can be another factor that contributes to less accurate fitting of the 38 nm sample. Additionally, for all the four samples, the value of *D* is about 10 percent of *C*. It shows higher contribution of the three-phonon effect compared with the four-phonon effect on temperature dependent Raman shift of the A_{1g} mode. This conclusion is in very good agreement with previous work conducted by Huang *et al* [29].

As mentioned earlier, α_{WS_2} is the volumetric thermal expansion coefficient of the WS_2 layer, while we need to know the linear thermal expansion in the in-plane direction of the supported sample in order to find the elongation of the sample. The linear thermal expansion coefficient of TMD structures in both in-plane and cross-plane directions obeys the following equations [59]:

$$\frac{\alpha_{WS_2,\parallel}(T)}{\alpha_{WS_2,\perp}(T)} = \frac{\langle \gamma_{\parallel}(T) \rangle}{\langle \gamma_{\perp}(T) \rangle}, \tag{13}$$

$$2\alpha_{WS_2,\parallel}(T) + \alpha_{WS_2,\perp}(T) = \alpha_{WS_2}(T), \tag{14}$$

where $\alpha_{WS_2,\parallel}$ and $\alpha_{WS_2,\perp}$ are in-plane and cross-plane linear thermal expansion coefficient, respectively. Additionally, $\langle \gamma_{\parallel}(T) \rangle$ and $\langle \gamma_{\perp}(T) \rangle$ indicate the mean Grüneisen constant in both directions, that are 0.9176 and 2.1707, respectively [59]. The in-plane linear temperature-dependent thermal expansion coefficient of the WS_2 samples are calculated using Eqs. (11) and (13-14) and fitted parameters c_0 and c_1, and are plotted as shown in Figure 7(a). The aforementioned discrepancy between the 38 nm sample's $\alpha_{WS_2,\parallel}$ and other samples is obvious in this figure, too. The range of $\alpha_{WS_2,\parallel}$ is about 5×10^{-6} to 8×10^{-6} K^{-1} at temperatures from 300 to 700 K, which is in

good agreement with reference values [29, 59, 60]. Huang *et al.* reported the in-plane thermal expansion coefficient of WS_2 as around 4.5×10^{-6} K^{-1} at 300 K, and 5×10^{-6} K^{-1} at 400 K [29]. Zhan-Yu *et al.* measured it as 6×10^{-6} K^{-1} for monolayer WS_2 for a wide temperature range from 400 to 800 K [60]. Now, using the known $\alpha_{WS_2,\|}$ and α_{Si} (from references) it is possible to estimate the expanded length of the WS_2 layer at each temperature as:

$$L(T) = L_0[1+\int_{RT}^{T}(\alpha_{WS_2,\|} \quad ^{\cdot\cdot})dT], \tag{15}$$

where L_0 is the initial length of the arbitrary sample and takes 10 μm in our estimation. The estimated length of each sample at different temperatures is shown in Figure 7(b). It shows that for all of the samples, the maximum elongation is around 13 nm when the temperature is increased from 300 K to 700 K. The average thickness of air layer [t_2 in inset of Figure 7(b)] is calculated and shown in Figure 8(a). For all of the samples, the theoretical thickness of air layer at maximum temperature is around 40 nm. This calculated air gap thickness is theoretical since there are other effects that can affect size of t_2, such as the debris and residues on Si substrate and structure of each sample that can restrain the elongation of the sample. Therefore, this estimated theoretical t_2 is the maximum value of the air layer spacing, while in the real case it will be smaller.

5.3. Effect of temperature dependent refractive index

Using the estimated spacing (t_2), and assuming that refractive index and extinction coefficient of WS_2 and Si increase by a certain amount as the temperature increases from 300 K to 700 K, the Raman intensity enhancement factor at each temperature could be calculated using Eq. (7) and (8). As mentioned earlier, these two equations only include the effect of air gap layer and change in refractive index on Raman intensity, and are totally independent of the effect of resonance Raman. Note that refractive index ($\tilde{i}$) is a function of both electronic band structure and thermal expansion

coefficient at higher temperatures, and it is increased by increased temperature [35]. Li *et al.* reported the temperature dependent refractive index of Si under laser irradiation with several wavelengths, and showed that $\tilde{\imath}$ increased by less than 5% under all laser conditions over a 500 K temperature rise from 300 to 800 K [61]. Since there is no reference value for the temperature dependent $\tilde{\imath}$ of WS_2, and to avoid more complexities, we assume that $\tilde{\imath}$ of both WS_2 and Si increases by 5% from RT to 700 K. In this work, our aim is to investigate how the increment of $\tilde{\imath}$ affects the Raman intensity enhancement factor, regardless of its actual value at each temperature. Fairness of this assumption will be evaluated in the following sections.

Figure 8 (b-d) show the Raman intensity enhancement factor (F) of the three thinner samples as a function of spacing (t_2) and $\Delta\tilde{\imath}$, where both are functions of temperature. For the 13 nm-thick sample, F mostly depends on spacing and increases as the air gap layer becomes wider, until t_2 reaches ~25 nm. At higher t_2 values, it decreases with increased $\Delta\tilde{\imath}$. For the other two samples, the relationship between F and t_2 is not uniform, and it decreases with increased t_2, and after a certain point, it starts to increase. For these two samples, F is lower at higher $\Delta\tilde{\imath}$ values, which is consistent with the 13 nm sample. Note that for the bulk sample, since it is very thick, the light cannot pass through the sample and regardless of the spacing, no interface interference effect will be observed. Comparing the three contours represented in Figure 8, it is clear that the estimated F of the 13 nm sample for a spacing layer more than about 5 nm is much more than the other three samples. This is in contrast with the fact that the higher the thickness of the sample, the more will be the F value. In fact, for the similar optical and electronic band properties, thermal expansion coefficient, and t_2, F only depends on t_1, and it reaches its maximum value for the bulk material. Therefore, we can conclude that the actual increment of the air layer thickness between the 13 nm

sample and substrate is less than the theoretical value as shown in Figure 8(a).

To further illustrate this effect, F versus temperature is calculated as shown in Figure 9(a). In this plot, F at each temperature carries the information about both refractive index and t_2 at that temperature. The blue line corresponds to F_{Bulk}, and is higher than the 38 nm sample. Regarding the 45 nm sample, it is very close to the bulk values. However, the Raman intensity of the 13 nm sample increases drastically with increased temperature. Figure 9(b) shows the normalized value of enhancement factor (F^*), which is calculated as: $F^* = F / F_{Bulk}$. As shown in this figure, F^* of 38 nm sample is less than 1, and for the 45 nm sample is very close 1 at different temperatures, and is in very good agreement with the experimental result as shown in Figure 6. In contrast to these two samples, F^* of the 13 nm one is much more than the bulk one at temperatures higher than 400 K, which does not agree with the experimental data. It points out that the theoretical estimation of t_2 for the 13 nm sample should be less than the real value.

To evaluate the assumption that $\tilde{\imath}$ is changed 5% over 400 K temperature rise, three different values of $\Delta\tilde{\imath}$ are used to calculate the F^* of the three samples and compare them to the former result that is shown as Figure 9(b). Figure 10(a) and (b) shows this calculation using $\Delta\tilde{\imath}$ equal to 2%, 8%, which means considering 60% uncertainty in our first assumption. Comparing Figure 9(b) to Figure 10(a) and (b), it is obvious that F^* of the 13 nm sample decreases with increased $\Delta\tilde{\imath}$. For the other two samples, this trend is totally reversed, and F^* takes higher values as $\Delta\tilde{\imath}$ increases. A new parameter F_N^* is introduced as: $F_N^* = F_{x\%}^* / F_{5\%}^*$, where x could take 2 or 8, to show the uncertainty caused on final F^* value in these two recent cases with regard to the F^* that is calculated using the 5% assumption. Figure 10(c) shows the result of this estimation. For both 2% and 8%

assumptions, and for all three samples, the uncertainty is 20% at most, which indicates that the first assumption is reasonable. Considering this point and the contours that were shown in Figure 8, we can conclude that the spacing caused between WS_2 and Si layer possesses more significant effect on Raman intensity than the change of optical properties with temperature.

It should be noted that the effect of refractive index is more challenging to be considered solely. We can design the experiment in a way to have this effect more significant compared with other effects by using thicker (bulk) samples. By doing so, the thermal stresses and interface optical interference effects will be minimized. Also, we can eliminate the resonance effect by choosing a laser whose photon energy is far from the excitonic transition energy of WS_2 samples. For instance, in a work by Fan *et al.* [33], several lasers with different wavelengths in a range of 488 to 633 nm are used to study the resonance Raman effect of several materials. They used a 594 nm laser with energy of about 2.09 eV which is far from the excitonic transition energy of B exciton of WS_2, as shown in our work in the temperature range from 77 to 300 K. Another effective way to mitigating the effect of resonance Raman is to find a material that its excitonic transition energy is very far from the laser's photon energy (2.33 eV in this work). Then there will be very weak effect of resonance Raman on the temperature dependent Raman intensity. As a result, the only parameter that contributes to Raman intensity will be the refractive index of the sample. However, in order to investigate this effect more quantitatively, it is necessary to include more information with greater accuracy. For example, as shown in the work by Cherroret *et al.* [35], it is possible to measure the temperature dependent refractive index of different materials, which needs information about other parameters, such as the temperature dependent electronic band structure at constant pressure and constant volume. The study of temperature dependent refractive index of nm-thick and bulk

WS_2 samples could be a topic of interesting research. When those data are available, it will be feasible to include the precise value of refractive indices in Raman intensity enhancement calculation to explore the effects of refractive index more accurately and quantitatively.

Another point that needs to be considered is the effect of laser heating and local temperature rise of the samples on our experiment and conclusions. Here, 3D modeling based on control volume method is conducted to calculate the temperature rise of the samples under the laser heating at room temperature. In-plane and out-of-plane thermal conductivities of WS_2 at room temperature take 35 $W \cdot m^{-1} \cdot K^{-1}$ and 4 $W \cdot m^{-1} \cdot K^{-1}$, respectively [25]. Also, the interfacial thermal resistance between the WS_2 layer and Si substrate is assumed to be 5×10^{-8} $K \cdot m^2 \cdot W^{-1}$. This estimation is based on the previous work by our group to study the interfacial thermal resistance between MoS_2 and Si substrate[39]. The laser absorption depth inside the WS_2 layer is calculated as: $\tau_L = \lambda / 4\pi k$, where λ and k are incident laser wavelength and extinction coefficient under 532 nm laser irradiation, respectively. Here, τ_L is 47 nm. The thermal conductivity of the Si substrate is 148 $W \cdot m^{-1} \cdot K^{-1}$. Based on these thermal properties, and considering 2 μm radius size of the laser spot, the temperature rise of each sample is calculated. For 13, 38, 45 nm, and bulk samples, the average temperature rise within the laser spot is calculated as 2.9, 2.7, 7.6, and 18 K, respectively. As we can see, for the first three samples, this temperature rise is less than 2% of total temperature range of the experiment. Also, it should be noted that this estimation is based on the thermal properties at room temperature, while at lower temperatures, the thermal conductivity will be higher and these temperature rises will be lower. Regarding the bulk sample, the error caused by the heating effect on Raman intensity measurement and I^*-T data will be around 8% in average and will not affect our qualitative conclusions.

6. Conclusion

In this work, the Raman intensity variation with temperature for multilayered WS_2 was systematically studied under 2.33 eV laser irradiation. Tuning the sample temperature made it possible to study the resonance Raman effects of the B exciton of WS_2. Their excitonic transition energy and broadening parameter were evaluated in detail. It was shown that there are other effects that contribute to the Raman intensity temperature variation of each mode, such as interface optical interference and temperature dependence of optical properties. To analyze these two effects, the Raman intensity of multilayered samples was normalized to the bulk one to take out the resonance Raman effects. To investigate the interface optical interference effects, the linear thermal expansion coefficient of WS_2 layer was calculated to perform a first order analysis of the air layer thickness between WS_2 and Si substrate. Using this thermal expansion effect and presumed refractive indices increase of 5% in our temperature range, the interface optical interference effects were studied. It was found that the temperature dependent Raman intensity of WS_2 samples under 532 nm laser could not be interpreted only by the resonance Raman effects. Comparing interface optical interference with the temperature variation of refractive indices, the former one contributed more to the Raman intensity variation with temperature for WS_2 films.

Conflict of interest

All authors have no competing interests to declare.

Acknowledgement

Partial support of this work by National Science Foundation (CBET1930866 for X.W.) is gratefully acknowledged. Y.X. is grateful for the partial support of National Natural Science

Foundation of China (51906161).

Corresponding Author

*E-mail: ysxie@szu.edu.cn (Y. X.), xwang3@iastate.edu (X. W.) (001-515-294-8023)

References

1. W. Choi, N. Choudhary, G. H. Han, J. Park, D. Akinwande and Y. H. Lee, *Materials Today*, 2017, **20**, 116-130.
2. Y. Zhang, T.-R. Chang, B. Zhou, Y.-T. Cui, H. Yan, Z. Liu, F. Schmitt, J. Lee, R. Moore and Y. Chen, *Nature nanotechnology*, 2014, **9**, 111.
3. W. S. Yun, S. Han, S. C. Hong, I. G. Kim and J. Lee, *Physical Review B*, 2012, **85**, 033305.
4. Y. Xie, M. Han, R. Wang, H. Zobeiri, X. Deng, P. Zhang and X. Wang, *ACS nano*, 2019, **13**, 5385-5396.
5. N. Asli, A. Ehsan, J. Guo, P. L. Lai, R. Montazami and N. N. Hashemi, *Biosensors*, 2020, **10**, 6.
6. J. Guo, N. Asli, A. Ehsan, K. R. Williams, P. L. Lai, X. Wang, R. Montazami and N. N. Hashemi, *Biosensors*, 2019, **9**, 112.
7. A. Hanbicki, M. Currie, G. Kioseoglou, A. Friedman and B. Jonker, *Solid State Communications*, 2015, **203**, 16-20.
8. A. Ramasubramaniam, *Physical Review B*, 2012, **86**, 115409.
9. M. Amani, R. A. Burke, X. Ji, P. Zhao, D.-H. Lien, P. Taheri, G. H. Ahn, D. Kirya, J. W. Ager III and E. Yablonovitch, *ACS nano*, 2016, **10**, 6535-6541.
10. Y. Yoon, K. Ganapathi and S. Salahuddin, *Nano letters*, 2011, **11**, 3768-3773.
11. C. Lee, Q. Li, W. Kalb, X.-Z. Liu, H. Berger, R. W. Carpick and J. Hone, *science*, 2010, **328**, 76-80.
12. N. Huo, J. Kang, Z. Wei, S. S. Li, J. Li and S. H. Wei, *Advanced Functional Materials*, 2014, **24**, 7025-7031.
13. S. Z. Butler, S. M. Hollen, L. Cao, Y. Cui, J. A. Gupta, H. R. Gutiérrez, T. F. Heinz, S. S. Hong, J. Huang and A. F. Ismach, *ACS nano*, 2013, **7**, 2898-2926.
14. W. Zhang, Q. Wang, Y. Chen, Z. Wang and A. T. Wee, *2D Materials*, 2016, **3**, 022001.
15. F. Ceballos, M. Z. Bellus, H.-Y. Chiu and H. Zhao, *ACS nano*, 2014, **8**, 12717-12724.
16. R. Nemanich, J. Glass, G. Lucovsky and R. Shroder, *Journal of Vacuum Science & Technology A: Vacuum, Surfaces, and Films*, 1988, **6**, 1783-1787.
17. R. Wang, T. Wang, H. Zobeiri, P. Yuan, C. Deng, Y. Yue, S. Xu and X. Wang, *Nanoscale*, 2018, **10**, 23087-23102.
18. R. Yan, J. R. Simpson, S. Bertolazzi, J. Brivio, M. Watson, X. Wu, A. Kis, T. Luo, A. R. Hight Walker and H. G. Xing, *ACS nano*, 2014, **8**, 986-993.
19. Q. Li, Y. Li, X. Zhang, S. B. Chikkannanavar, Y. Zhao, A. M. Dangelewicz, L. Zheng, S. K. Doorn, Q. Jia and D. E. Peterson, *Advanced Materials*, 2007, **19**, 3358-3363.
20. H. Zobeiri, R. Wang, C. Deng, Q. Zhang and X. Wang, *The Journal of Physical Chemistry C*, 2019, **123**, 23236-23245.
21. P. Yuan, R. Wang, H. Tan, T. Wang and X. Wang, *ACS Photonics*, 2017, **4**, 3115-3129.
22. S. Sahoo, A. P. Gaur, M. Ahmadi, M. J.-F. Guinel and R. S. Katiyar, *The Journal of Physical Chemistry C*, 2013, **117**, 9042-9047.
23. X. Zhang, D. Sun, Y. Li, G.-H. Lee, X. Cui, D. Chenet, Y. You, T. F. Heinz and J. C. Hone, *ACS applied materials & interfaces*, 2015, **7**, 25923-25929.
24. R. Wang, H. Zobeiri, H. Lin, W. Qu, X. Bai, C. Deng and X. Wang, *Carbon*, 2019, **147**, 58-69.

25. H. Zobeiri, R. Wang, Q. Zhang, G. Zhu and X. Wang, *Acta Materialia*, 2019, **175**, 222-237.
26. P. Yuan, J. Liu, R. Wang and X. Wang, *Nanoscale*, 2017, **9**, 6808-6820.
27. D. J. Late, S. N. Shirodkar, U. V. Waghmare, V. P. Dravid and C. Rao, *ChemPhysChem*, 2014, **15**, 1592-1598.
28. L. F. Huang, P. L. Gong and Z. Zeng, *Physical Review B*, 2014, **90**, 045409.
29. X. Huang, Y. Gao, T. Yang, W. Ren, H.-M. Cheng and T. Lai, *Scientific reports*, 2016, **6**, 32236.
30. S. V. Bhatt, M. Deshpande, V. Sathe, R. Rao and S. Chaki, *Journal of Raman Spectroscopy*, 2014, **45**, 971-979.
31. E. Smith and G. Dent, *Modern Raman spectroscopy: a practical approach*, Wiley, 2019.
32. R. Loudon, *Proceedings of the Royal Society of London. Series A. Mathematical and Physical Sciences*, 1963, **275**, 218-232.
33. J.-H. Fan, P. Gao, A.-M. Zhang, B.-R. Zhu, H.-L. Zeng, X.-D. Cui, R. He and Q.-M. Zhang, *Journal of Applied Physics*, 2014, **115**, 053527.
34. A. P. Gaur, S. Sahoo, J. Scott and R. S. Katiyar, *The Journal of Physical Chemistry C*, 2015, **119**, 5146-5151.
35. N. Cherroret, A. Chakravarty and A. Kar, *Journal of materials science*, 2008, **43**, 1795-1801.
36. Y. Yue, J. Zhang, Y. Xie, W. Chen and X. Wang, *International Journal of Heat and Mass Transfer*, 2017, **110**, 827-844.
37. T. Wang, R. Wang, P. Yuan, S. Xu, J. Liu and X. Wang, *Advanced Materials Interfaces*, 2017, **4**, 1700233.
38. H. Zobeiri, R. Wang, T. Wang, H. Lin, C. Deng and X. Wang, *International Journal of Heat and Mass Transfer*, 2019, **133**, 1074-1085.
39. P. Yuan, C. Li, S. Xu, J. Liu and X. Wang, *Acta Materialia*, 2017, **122**, 152-165.
40. P. Yuan, H. Tan, R. Wang, T. Wang and X. Wang, *RSC Advances*, 2018, **8**, 12767-12778.
41. J. Verble and T. Wieting, *Physical review letters*, 1970, **25**, 362.
42. C. Sourisseau, F. Cruege, M. Fouassier and M. Alba, *Chemical physics*, 1991, **150**, 281-293.
43. C. Ho, C. Wu, Y. Huang, P. Liao and K. Tiong, *Journal of Physics: Condensed Matter*, 1998, **10**, 9317.
44. J. V. Acrivos, W. Liang, J. Wilson and A. Yoffe, *Journal of Physics C: Solid State Physics*, 1971, **4**, L18.
45. T. Livneh and E. Sterer, *Physical Review B*, 2010, **81**, 195209.
46. S. Sinha, V. Sathe and S. K. Arora, *Solid State Communications*, 2019, **298**.
47. Y. P. Varshni, *physica*, 1967, **34**, 149-154.
48. P. K. Sarswat and M. L. Free, *Physica B: Condensed Matter*, 2012, **407**, 108-111.
49. P. Lautenschlager, M. Garriga, S. Logothetidis and M. Cardona, *Physical Review B*, 1987, **35**, 9174.
50. P. Lautenschlager, M. Garriga, L. Vina and M. Cardona, *Physical Review B*, 1987, **36**, 4821.
51. X. Tang, S. Xu, J. Zhang and X. Wang, *ACS applied materials & interfaces*, 2014, **6**, 2809-2818.

52. D. Yoon, H. Moon, Y.-W. Son, J. S. Choi, B. H. Park, Y. H. Cha, Y. D. Kim and H. Cheong, *Physical Review B*, 2009, **80**, 125422.
53. I. V. Semiconductor, 2012.
54. H. Watanabe, N. Yamada and M. Okaji, *International journal of thermophysics*, 2004, **25**, 221-236.
55. L. Su, Y. Zhang, Y. Yu and L. Cao, *Nanoscale*, 2014, **6**, 4920-4927.
56. J. Menéndez and M. Cardona, *Physical Review B*, 1984, **29**, 2051.
57. S. El-Mahalawy and B. Evans, *Journal of Applied Crystallography*, 1976, **9**, 403-406.
58. M. Balkanski, R. Wallis and E. Haro, *Physical Review B*, 1983, **28**, 1928.
59. Y. Ding and B. Xiao, *RSC Advances*, 2015, **5**, 18391-18400.
60. W. Zhan-Yu, Z. Yan-Li, W. Xue-Qing, W. Fei, S. Qiang, G. Zheng-Xiao and J. Yu, *Chin. Phys. B*, 2015, **24**, 026510.
61. H. Li, *Journal of Physical and Chemical Reference Data*, 1980, **9**, 561-658.

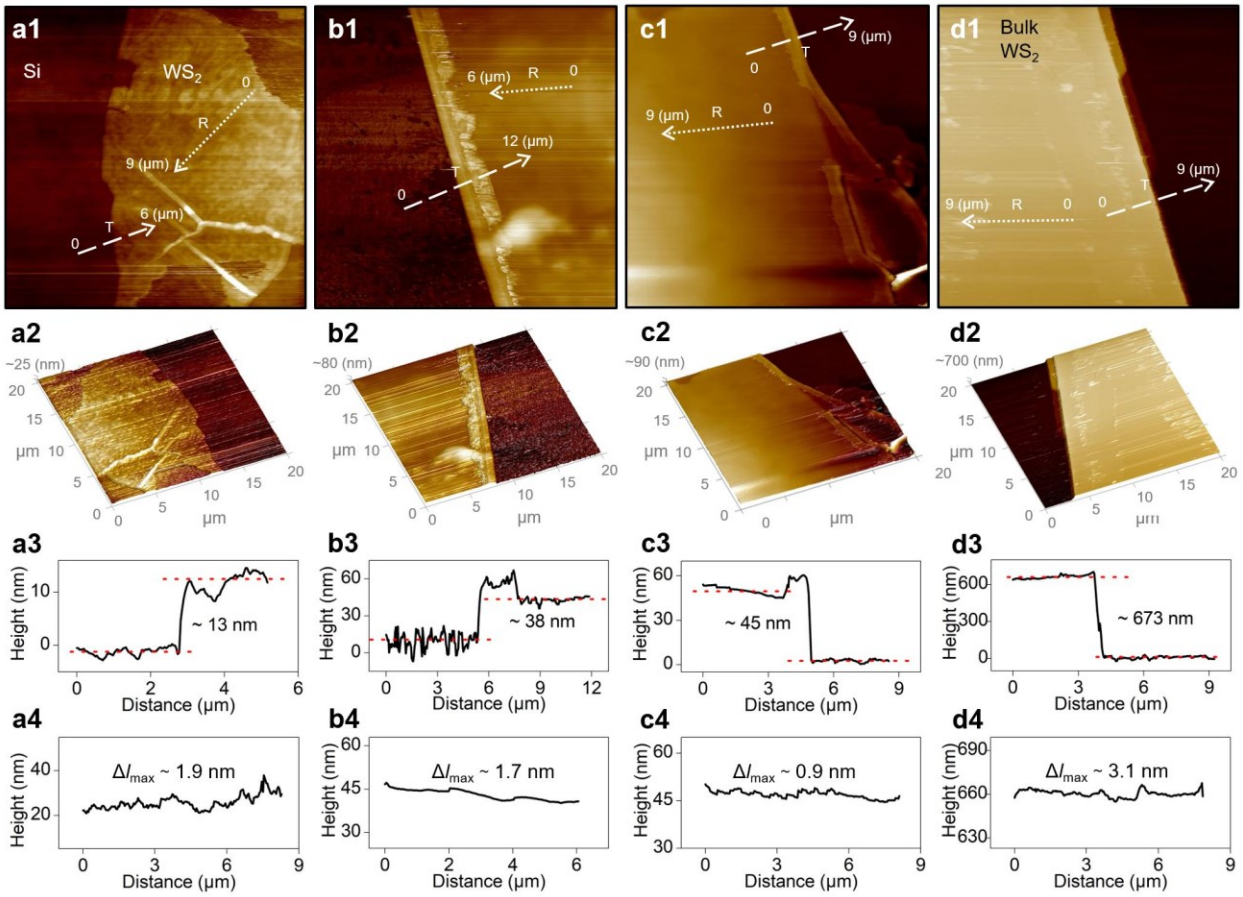

Figure 1. AFM imaging of the four supported WS_2 samples. (a1-d1) 2D AFM images of all samples. (a2-d2) 3D AFM images of all samples. (a3-d3) Thickness profile of the samples that correlates to the white dashed arrows (labeled by T). (a4-d4) Roughness profile on the surface of WS_2 that corresponds to the white dotted arrows (labeled by R). These dotted arrows cover the location of laser spot.

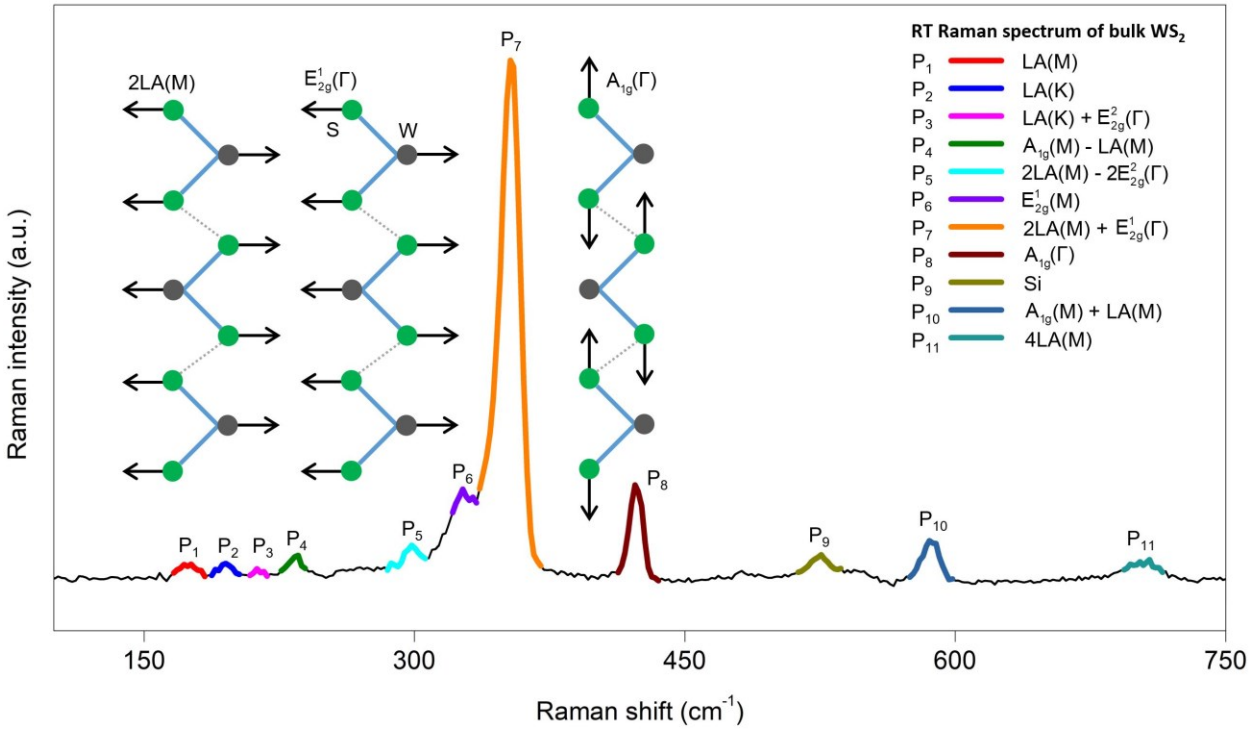

Figure 2. Raman spectrum of the bulk WS_2 sample collected with 532 nm near resonance laser at room temperature. Three main vibrational modes between WS_2 layers are depicted and labeled as P_i, where i is the peak number, and green and black balls represent the sulfur and tungsten atoms, respectively. The gray dashed lines between each layer of material show the weak van der Waals forces.

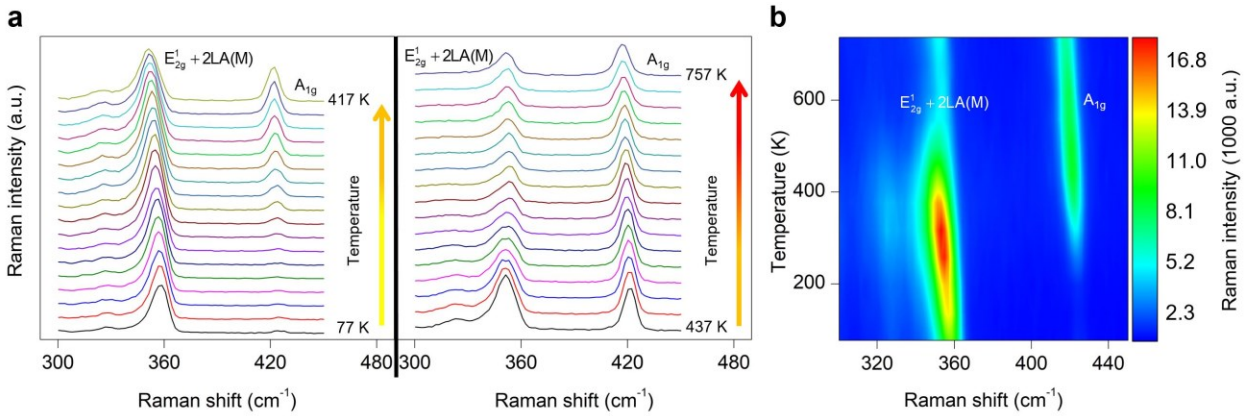

Figure 3. Temperature dependent Raman intensity of bulk WS_2 from 77 to 757 K indicated as (a) Raman spectrum, and (b) 2D contour, in the range of 300 to 450 cm^{-1}. The resonant Raman effect is observable with the increased temperature of the sample and gradual increase of the Raman intensity of both peaks in midrange temperature, and its decrease at higher temperatures.

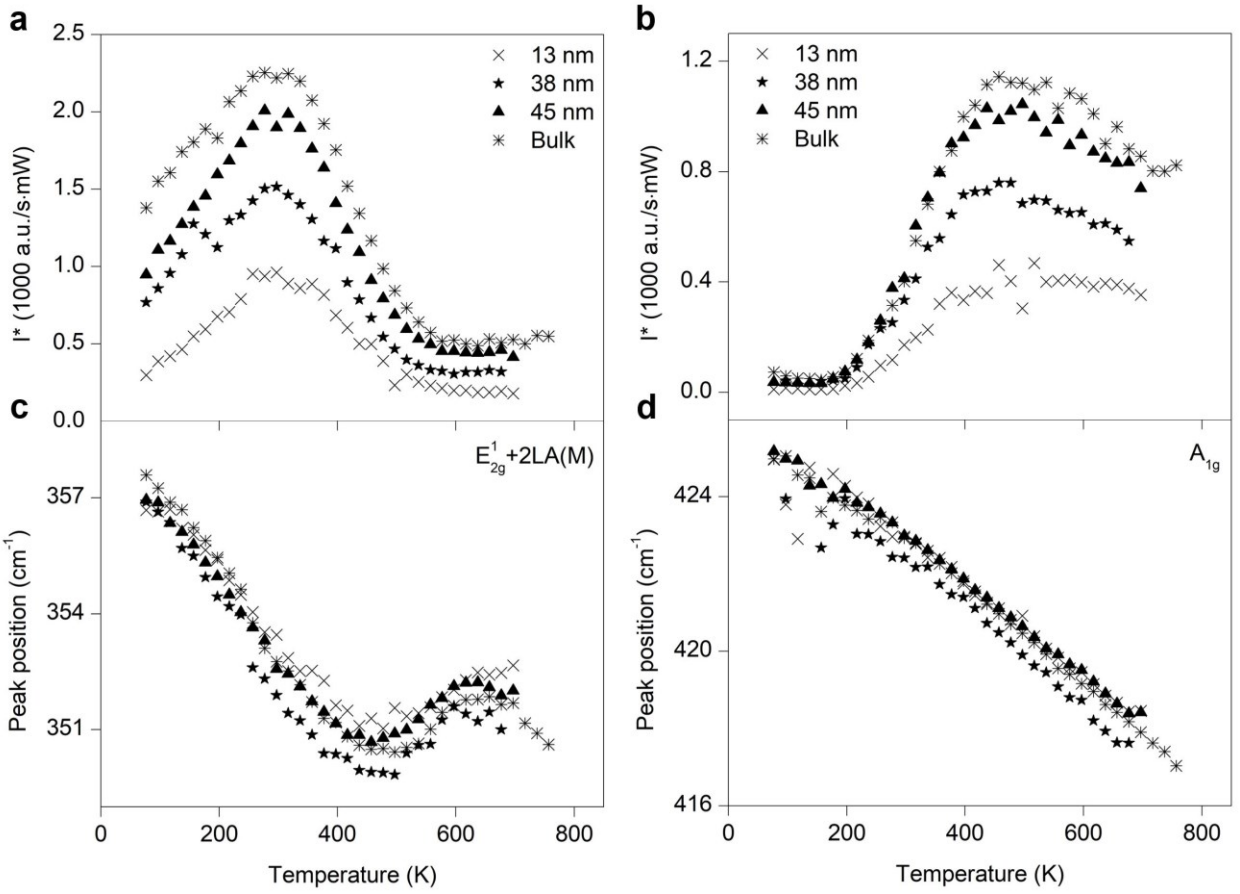

Figure 4. (a) and (b) show the temperature dependent Raman intensity of combined $E^1_{2g}+2LA(M)$ and A_{1g} modes of all four samples, respectively. For both cases, the Raman intensity reaches the maximum value at around 350 K. For each Raman mode, as the sample thickness increases, the I^* at each temperature increases, too. This behavior is attributed to the optical interference effect inside the WS_2 layers and between the WS_2 layer and Si substrate. (c) and (d) show the temperature dependent Raman peak position of $E^1_{2g}+2LA(M)$ and A_{1g} modes, respectively. The nonlinearity of $E^1_{2g}+2LA(M)$ curve is caused by the combined effects of 2LA(M) and E^1_{2g} mode. The 2LA(M) peak is dominant at low temperatures. As the temperature increases, the E^1_{2g} mode becomes stronger and contributes more to the combined mode. This behavior is obvious at temperatures close to 450 K, where the peak position indicates a blue shift which means at temperatures more than 450 K, Raman intensity of 2LA(M) is less than that of the E^1_{2g} mode and is not affecting the Raman intensity of combined mode significantly. The temperature dependent Raman peak position of A_{1g} mode for all four samples is almost linear for all temperatures and is consistent with the reference values. For the 13 nm sample, the peak position does not follow the linear trend perfectly. This could be caused by experimental and fitting errors, and surface non-uniformity at different temperatures.

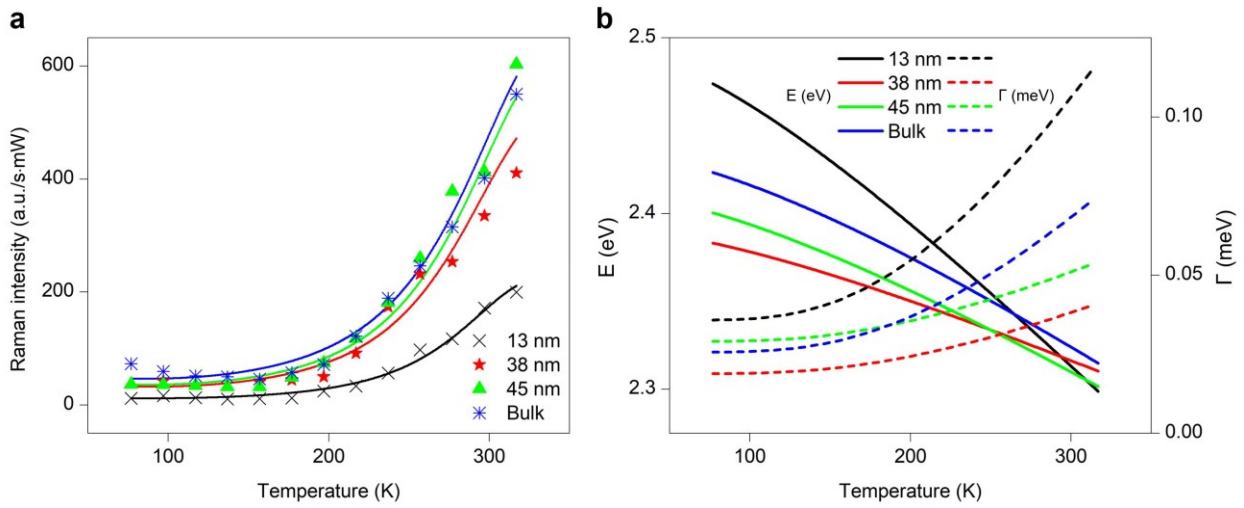

Figure 5. (a) Experimental data of Raman intensity of the A_{1g} peak of each sample in the range of temperatures less than 320 K is shown by symbols, and the fitted values are shown using solid lines. (b) Theoretical values of E (left vertical axis) and Γ (right vertical axis) which are calculated using the fitted parameters and Eqs. (5) and (6). Solid and dashed lines represent the E and Γ values, respectively.

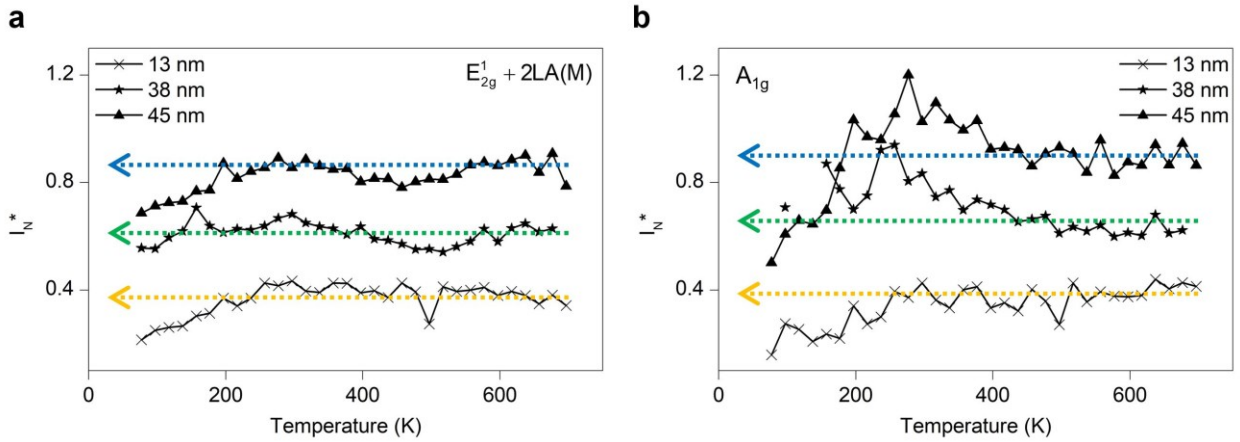

Figure 6. Raman intensity of the three few-layered samples is normalized using the Raman intensity of bulk sample at each temperature in order to take out the resonant Raman effects. Dotted arrows indicate the approximate average value of I_N^* over the all temperature range. For both $E^1_{2g} + 2LA(M)$ and A_{1g} modes, these values are very close for a specific sample. It shows that regardless of the Raman mode, I_N^* only carries the information about the optical (*n* and *k*) and interfaces spacing effects.

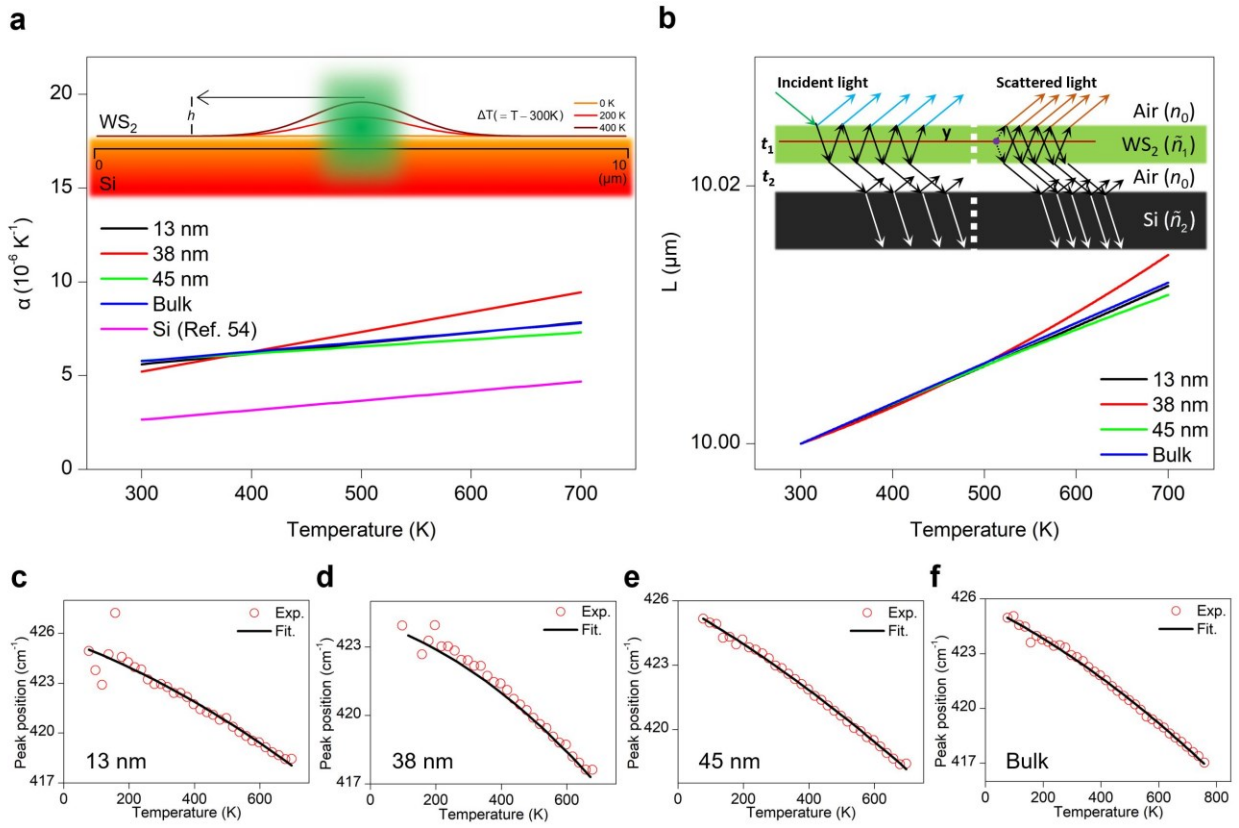

Figure 7. (a) Estimated temperature-dependent linear thermal expansion coefficient of four supported WS_2 samples. Inset of this figure shows the elongation of the WS_2 layer due to the temperature rise and thermal expansion mismatch between the sample and substrate to show the air gap spacing caused at higher temperatures. Here, only the linear elongation of the sample along a 10 μm line is considered to estimate the thickness of spacing. Due to Gaussian distribution of the laser energy, it is assumed that WS_2 layer will expand in Gaussian form, too. (b) Length of each sample as a function of temperature. The inset shows the concept of the multi-reflection phenomenon inside the layers of WS_2, air, and Si. t_1 and t_2 are the thickness of WS_2 layer and air gap, respectively. Left and right sides of the white dotted line correspond to the absorption and scattering processes, respectively. (c)-(d) show the fitting process that is conducted to explore the effects of thermal expansion and phonon anharmonicities variations and their contribution to frequency shift of the A_{1g} mode. Hollow red points and solid black lines represent the experimental data and their fitted values, respectively. Lower fitting quality of the 38 nm sample could be caused by the stronger non-linear behavior of the frequency shift in comparison with other three samples.

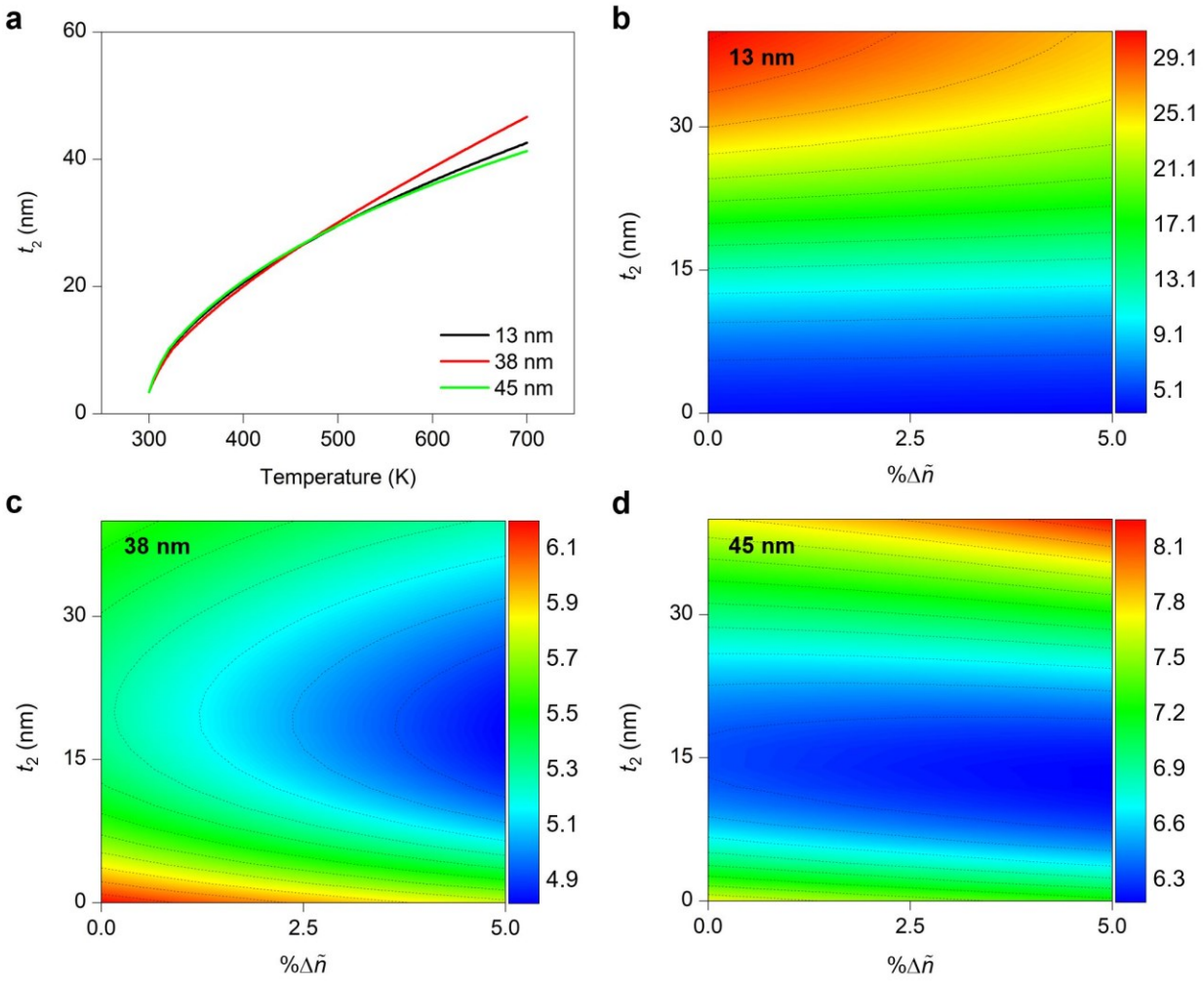

Figure 8. (a) Thickness of the air gap layer as a function of temperature. t_2 is calculated as the average of height [h in inset of Figure 7(a)] of Gaussian shape of the expanded layer over a 10 μm line. (b)-(d) 2D contour of F versus $\Delta\tilde{i}$ and t_2. All of these four contours are plotted based on the assumption that refractive index of the materials increases 5% over a 400 K temperature rise from 300 to 700 K.

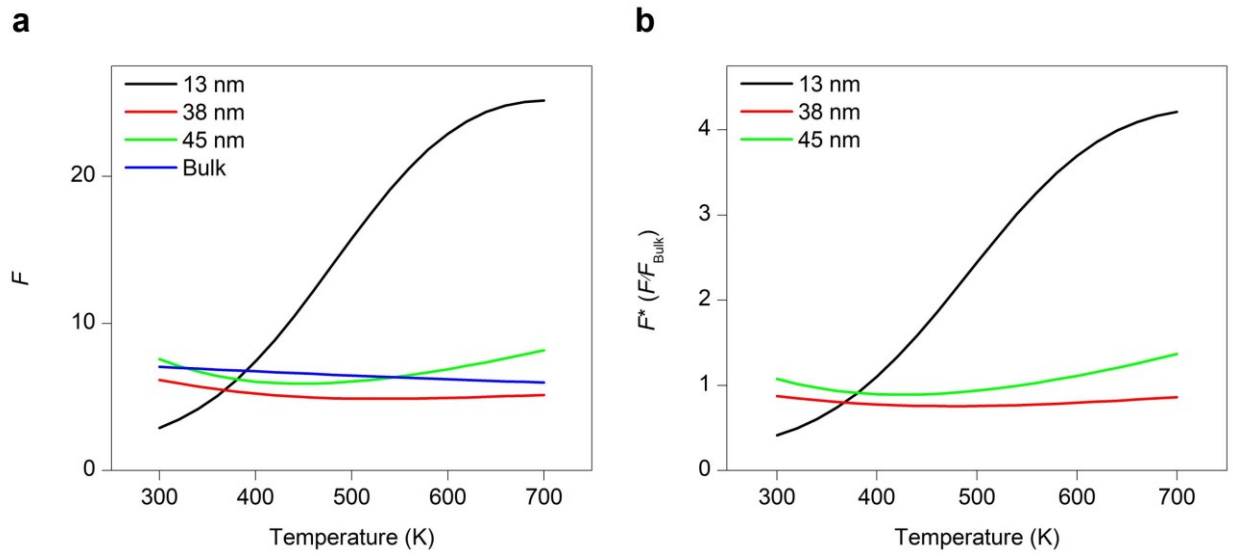

Figure 9. (a) Raman intensity enhancement factor (F) as the function of T. This plot includes the effects of both optical properties evolution and thermal expansion at higher temperatures. (b) F^* shows the normalized F with respect to F_{Bulk}. Note that spacing (t_2) values that are used in this calculation are based on theoretical values [Figure 8(a)], which are obviously not consistent with the experimental I_N^*, as shown in Figure 6(b).

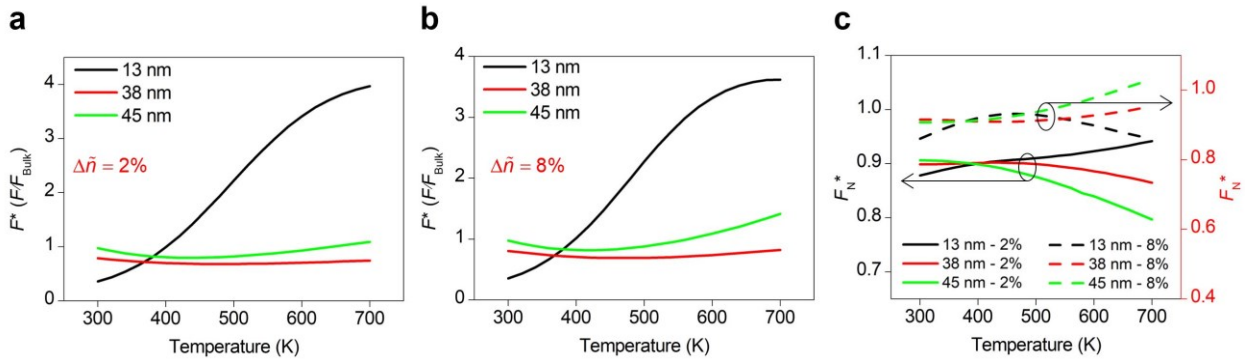

Figure 10. (a) and (b) The estimated F^* using the assumption that $\tilde{n}$ increases 2% and 8% over the 300 to 700 K temperature range, respectively. The default value that is used in previous discussion is 5%. Therefore, these two plots represent the F^* value that is estimated with 60% uncertainty comparing to the default assumption. (c) The calculated F_N^* regarding the 2% (left vertical axis) and 8% (right vertical axis). When the temperature is less than 500 K, the uncertainty of the F^* for both recent assumptions is less than 10%, and for higher temperatures, it does not exceed 20%.